The Significance of the Influence of the CME Deflection in Interplanetary Space on the CME Arrival at Earth

Bin Zhuang[1,2] , Yuming Wang[1,3], Chenglong Shen[1,3,4], Siqing Liu[5,6], Jingjing Wang[5,6], Zonghao Pan[1,4], Huimin Li[7], and Rui Liu[1,2,4]

[1] CAS Key Laboratory of Geospace Environment, Department of Geophysics and Planetary Sciences,
University of Science and Technology of China, Hefei 230026, China; ymwang@ustc.edu.cn
[2] Collaborative Innovation Center of Astronautical Science and Technology, Hefei 230026, China
[3] Synergetic Innovation Center of Quantum Information and Quantum Physics, University of Science and Technology of China, Hefei 230026, China
[4] Mengcheng National Geophysical Observatory, School of Earth and Space Sciences, University of Science and Technology of China, Hefei 230026, China
[5] National Space Science Center, Chinese Academy of Sciences, Beijing, China
[6] University of Chinese Academy of Sciences, Beijing, China
[7] Network and Information Center, University of Science and Technology of China, Hefei 230026, China

Abstract

As one of the most violent astrophysical phenomena, coronal mass ejections (CMEs) have strong potential space weather effects. However, not all Earth-directed CMEs encounter the Earth and produce geo-effects. One reason is the deflected propagation of CMEs in interplanetary space. Although there have been several case studies clearly showing such deflections, it has not yet been statistically assessed how significantly the deflected propagation would influence the CME's arrival at Earth. We develop an integrated CME-arrival forecasting (iCAF) system, assembling the modules of CME detection, three-dimensional (3D) parameter derivation, and trajectory reconstruction to predict whether or not a CME arrives at Earth, and we assess the deflection influence on the CME-arrival forecasting. The performance of iCAF is tested by comparing the two-dimensional (2D) parameters with those in the Coordinated Data Analysis Workshop (CDAW) Data Center catalog, comparing the 3D parameters with those of the gradual cylindrical shell model, and estimating the success rate of the CME Earth-arrival predictions. It is found that the 2D parameters provided by iCAF and the CDAW catalog are consistent with each other, and the 3D parameters derived by the ice cream cone model based on single-view observations are acceptable. The success rate of the CME-arrival predictions by iCAF with deflection considered is about 82%, which is 19% higher than that without deflection, indicating the importance of the CME deflection for providing a reliable forecasting. Furthermore, iCAF is a worthwhile project since it is a completely automatic system with deflection taken into account.

Key words: Sun: coronal mass ejections (CMEs)

1. Introduction

Coronal mass ejections (CMEs) are some of the most violent events in interplanetary space, carrying a huge amount of energy, and capable of producing geomagnetic storms (Gosling et al. 1990; Srivastava & Venkatakrishnan 2004) and other space weather phenomena if they arrive at Earth. It was once thought that frontside halo CMEs, which originate from the solar source region facing the Earth, would propagate along the Sun–Earth line (e.g., Howard et al. 1982) and arrive at Earth. However, not all CMEs can hit the Earth; the ratio is about 65%–80% (Wang et al. 2002; Yermolaev & Yermolaev 2006, and references therein). On the contrary, some limb CMEs may encounter the Earth (Webb et al. 2000; Zhang et al. 2003; Cid et al. 2012). The CME deflection in both coronae and interplanetary space is believed to be one of the reasons for this variation. The CME on 2008 September 13 is found to be deflected by more than 20° toward the west in interplanetary space (Wang et al. 2014); the unexpected and largest geomagnetic storm so far in solar cycle 24, referred to as the 2015 St. Patrick's Day event, was caused by a CME that was initially west-oriented and then deflected toward the Earth, increasing its geoeffectiveness (Wang et al. 2016). However, it has never been assessed how significantly such deflections can influence the CME Earth-arrival forecasting despite deflection events often being reported (Wang et al. 2006; Kilpua et al.

2009; Isavnin et al. 2014; Möstl et al. 2015). Therefore, we have developed a CME Earth-arrival forecasting system with CME deflection taken into account. By comparing the success rates of the forecasting with/without the deflection module, we can learn how important the deflection is to influencing the CME arrival at the Earth.

To forecast the Earth-arrival of a CME, the first step is to find whether or not there is a CME and how large the CME angular extent is. A direct method is to use coronagraph observations, such as the Large Angle and Spectrometric Coronagraph (LASCO; Brueckner et al. 1995) on board the *Solar and Heliospheric Observatory* (*SOHO*), or the Sun-Earth Connection Coronal and Heliospheric Investigation (Howard et al. 2008) of the *Solar Terrestrial Relations Observatory* (*STEREO*; Kaiser et al. 2008). The identification and cataloging of the observational CMEs is a primary task. There is a LASCO CME catalog at the Coordinated Data Analysis Workshop (CDAW) Data Center (http://cdaw.gsfc.nasa.gov/CME_list) that provides two-dimensional (2D) projected parameters of CMEs, including the first-appearance time in a LASCO/C2 field of view (FOV), the speed, the central position angle (CPA), and the angular width (AW; Yashiro et al. 2004). However, this CDAW catalog is generated and maintained by humans, which does not meet the needs of real-time forecasting. In addition to manual inspection, several automatic CME detection methods have been developed. The

Computer Aided CME Tracking (CACTus) software package (Berghmans et al. 2002; Robbrecht & Berghmans 2004; online at http://sidc.oma.be/cactus) is an effective method to detect CMEs based on coronagraph images; the package implements the image-processing technique of the Hough transform, and has detected about 94% of the CMEs in the CDAW catalog from 2003 November 9 to 14. Olmedo et al. (2008) have proposed another automatic CME detection method called SEEDs, whose algorithm is based on a 2D to 1D projection method where CMEs are assumed to be bright features moving radially outward as observed in running difference images. SEEDs detected about 75% of the CMEs in the CDAW catalog, but it picked up about 100% more small-size or anomalous transient features, which limits the application of this method for real-time CME detection. Other methods have been proposed as well: Liewer et al. (2005) developed a technique using two sequential coronagraph images based on tracking arc-like features; Qu et al. (2006) used image enhancement, segmentation, and morphological methods to detect and characterize CME regions; Byrne et al. (2011, 2012) utilized a multiscale edge-detection algorithm to separate the dynamic CME signal from the background corona and then detect the CMEs. However, no detailed performance on these detection methods was reported.

When a CME expands into interplanetary space, its shape roughly remains self-similar (Plunkett et al. 1998; Schwenn et al. 2005), i.e., its AW is almost a constant. Usually there are only single-view observations to provide 2D information in the plane-of-the-sky; some authors have suggested that the three-dimensional (3D) parameters of a CME may be derived by fitting a cone to the 2D CME images (Howard et al. 1982; Fisher & Munro 1984; Zhao et al. 2002; Michałek et al. 2003; Xie et al. 2004; Michalek 2006). Xue et al. (2005) used an ice cream cone model to estimate CME 3D parameters by fitting the projected speeds measured in LASCO FOV. These 3D parameters include the radial speed, the AW of the cone, and the direction of the cone axis, which demonstrates the CME propagation direction in the corona. The ice cream cone model can be applied to both halo and non-halo CMEs. Since CMEs are believed to have a flux-rope topology (Chen et al. 1997; Dere et al. 1999; Forbes 2000; Chen & Krall 2003; Vourlidas et al. 2013), a more realistic model is the gradual cylindrical shell (GCS) model (Thernisien et al. 2006, 2009; Thernisien 2011). The ice cream cone model is a special case of the GCS model where two legs of the GCS flux rope overlap completely. The GCS model was applied widely after the launch of the twin *STEREO* spacecraft when multiple-viewpoint observations became available. It uses six free parameters to shape the flux rope, including the height or heliocentric distance of the leading edge, the latitude and longitude of the propagation direction, face-on and edge-on angular widths, and the tilt angle of the main axis. In the work of Lee et al. (2015b), it was found that the radial speeds and propagation directions of halo CMEs fitted by both the ice cream cone model and the GCS model were consistent with one another; the correlation coefficients of the two sets of the above parameters are greater than 0.9. However, the ice cream cone AWs were systematically smaller than the GCS flux rope face-on widths, and they found that the correlation coefficient of the two sets of AWs is only about 0.29. They attributed their inconsistency to the fits of the widths in two models: the GCS model is applied to fit the body of a CME, while the ice cream cone model is

applied to fit the CME shock structure. Roughly, for the purpose of forecasting the CME arrival based on single-view observations, the ice cream cone is still an appropriate assumption and can be used.

Although the direction of a CME in the corona can be derived from the coronagraph images, it may change during the propagation in interplanetary space (Wang et al. 2004, 2006; Kilpua et al. 2009; Lugaz 2010; Rodriguez et al. 2011; Wang et al. 2014, 2016), which may influence CME Earth-arrival forecasting, as we mentioned earlier. Wang et al. (2004) proposed that an isolated CME traveling with a speed different from that of the ambient solar wind will be deflected due to the pileup of solar wind plasma ahead or behind the CME. CMEs can also experience deflection due to CME–CME interaction (Wang et al. 2011; Lugaz et al. 2012; Shen et al. 2012). The deflection angle of a CME in interplanetary space could reach 10° or even larger. Moreover, the solar wind will force the CME to accelerate or decelerate and further influence its arrival time (Gopalswamy et al. 2000; Cargill 2004; Manoharan 2006; Subramanian et al. 2012, 2014; Sachdeva et al. 2015). It should be noted that the deflection itself can also influence the CME-arrival time at Earth due to the curved front of the CME (Möstl et al. 2014; Shen et al. 2014).

Until now, there has been no completely automatic system with deflection taken into account that forecasts the Earth-arrival of a CME. Some methods are concentrated on the CME-arrival time (see Zhao & Dryer 2014; Hess & Zhang 2015; Mays et al. 2015; Shi et al. 2015; Rollett et al. 2016; Vršnak et al. 2016). The Wang–Sheeley–Arge (WSA)/ENLIL+Cone model, which is installed at the Community Coordinated Modeling Center (CCMC), and executed in real-time at the CCMC/Space Weather Research Center, can provide 1–4 day advance warning of Earth-directed CMEs and corresponding geomagnetic storms. This model assembles a time-dependent 3D magnetohydrodynamic (MHD) model of the heliosphere (called ENLIL; Odstrcil & Pizzo 1999), an empirical WSA coronal model (Arge & Pizzo 2000), and a cone model (Xie et al. 2004). However, the human input of the CME parameters makes it difficult to maintain the real-time arrival forecasting. We develop an integrated CME-arrival forecasting (iCAF) system, that assembles the modules of CME detection, 3D parameter derivation, and trajectory reconstruction. Although iCAF only predicts whether or not a CME arrives, without an arrival time, it is still a worthwhile project, as its operation is completely automatic and deflection is taken into account. Currently, iCAF is designed to apply to single-view observations from instruments orbiting at the L1 Lagrangian point (such as *SOHO*/LASCO), which is a regular position for a space weather monitor.

In Section 2, we introduce the modules of iCAF. In Section 3, we test the performance of the modules and assess the significance of the CME deflection for CME-arrival forecasting. We provide our conclusions and a discussion in Section 4.

2. Modules of iCAF

Figure 1 shows the flowchart of iCAF: the green rhombuses represent the modules, and the blue rectangles represent the inputs of the downstream module or the outputs of the upstream module. Starting from *SOHO*/LASCO coronagraph images, iCAF first detects CMEs and extracts the 2D projected parameters if a CME was detected. Then, the
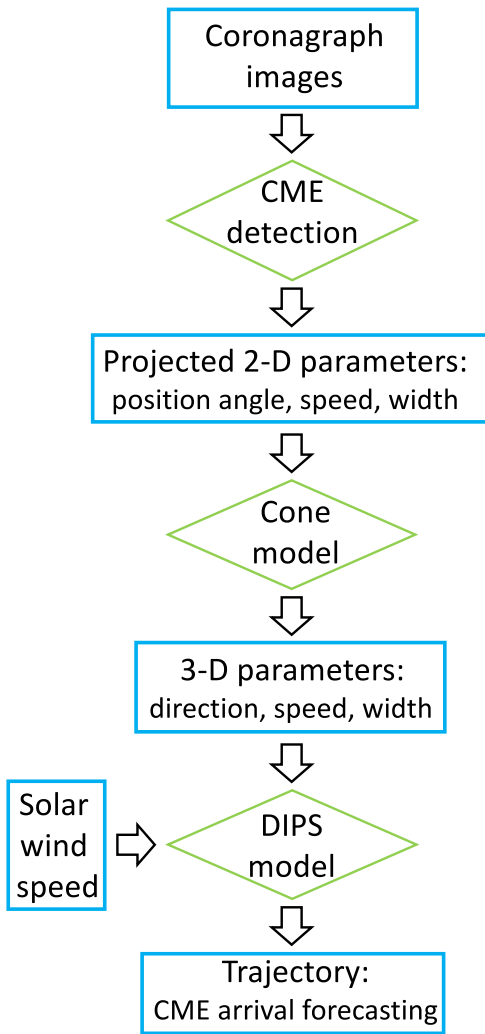
Figure 1. Flowchart of iCAF.

Figure 2. CME identification map. The temporal range is set according to the recognized first-appearance times of all the data points. The dashed rectangle encloses the cluster of the 2011 August 3 CME.

parameters are fitted by the ice cream cone model to derive the 3D parameters. After that, iCAF uses the deflection model to reconstruct the trajectory of the CME in interplanetary space. The CME Earth-arrival forecasting is therefore achieved. Here, we use the halo CME on 2011 August 3 as an example to illustrate the complete iCAF procedure.

2.1. Module 1: CME Detection

As mentioned before, there have been many CME automatic detection methods and they have their own characteristics. SEEDs recognizes CMEs in every coronagraph image by setting some thresholds, and it can detect very weak CMEs at the cost of many false detections. To avoid such invalid detection results, iCAF uses the Hough transform technique (Jahne 1997) to recognize bright-ridge features of CMEs in time-height space (called Jmap; Sheeley et al. 1999; Davis et al. 2009), which is as same as the technique used in CACTus. This technique considers the temporal change of the CME features when detecting CMEs, which provides the CME kinematic information. If a Jmap at a position angle (PA) cuts through a CME, an inclined bright ridge will be seen (refer to Figure 14 in the Appendix). Based on it, iCAF sets thresholds to pick out some bright features including the ridge from Jmap to operate the Hough transform, and then extracts the linear
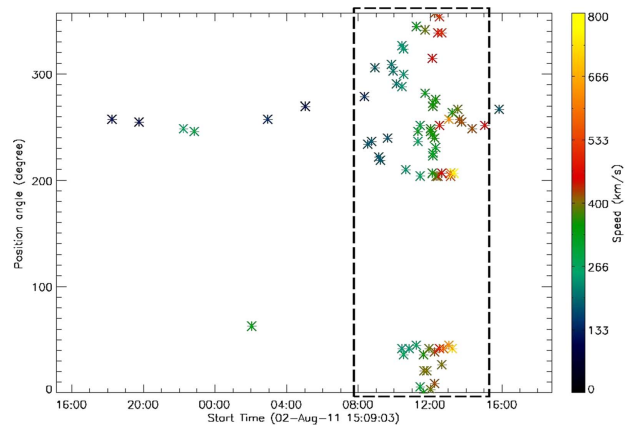
information of the ridge by setting another threshold. The projected speed and the first-appearance time in LASCO/C2 FOV along the PA are derived by a linear fit to the recognized CME feature. The resolution of the PA in this module is set to 3°, indicating that it will process 120 Jmaps at different PAs for the whole 360° in the plane-of-the-sky. Then, we use the speeds and first-appearance times for all the PAs to further identify CMEs. Figure 2 shows the data-point scattering in time and PA space, in which the speeds are scaled by the colors. Since the first-appearance time and the speed of a CME differ slightly from angle to angle, starting from a data point, iCAF finds the nearest data point whose speed is close to the initial data point and combines these two data points as a cluster. Then, from the cluster, iCAF repeats the above procedure to find the next data point that is close to the cluster and has a similar speed. The iteration stops when no data point can be found to be combined with the cluster. In Figure 2, the dashed rectangle encloses a cluster after the iteration, which is the 2011 August 3 CME. Although the rightmost data point is located near the cluster, it is not identified as a part of the cluster, because its speed is much smaller than that of the nearest one. Finally, iCAF derives the 2D projected parameters (the CPA, the AW, the first-appearance time in LASCO/C2 FOV, and the maximum speed) of the CME and tracks the CME in coronagraphs. The 2D parameters of the 2011 August 3 CME are 300°, 190°, 2011 August 3 13:12 UT, and 638 km s^{-1}. Figure 3 contains the tracking images in LASCO/C3 FOV, in which the blue symbols mark the auto-detected leading edge of the CME front, and most of which match the observations well. iCAF will discard the CME whose AW is smaller than 15°, or whose speed is slower than 100 km s^{-1}. Since our procedure at this step is similar to that of CACTus, we put a detailed description of this module in the Appendix for reference.

2.2. Module 2: 3D Parameter Derivation

iCAF uses the ice cream cone model (Xue et al. 2005) to derive the CME 3D parameters in the corona (the radial speed, the AW, the latitude, and longitude of the propagation direction) from 2D projected parameters. It requires us to input the projected speeds at different PAs, as well as input the eruption location on the solar surface. The first module can provide the projected speeds, but is unable to locate the
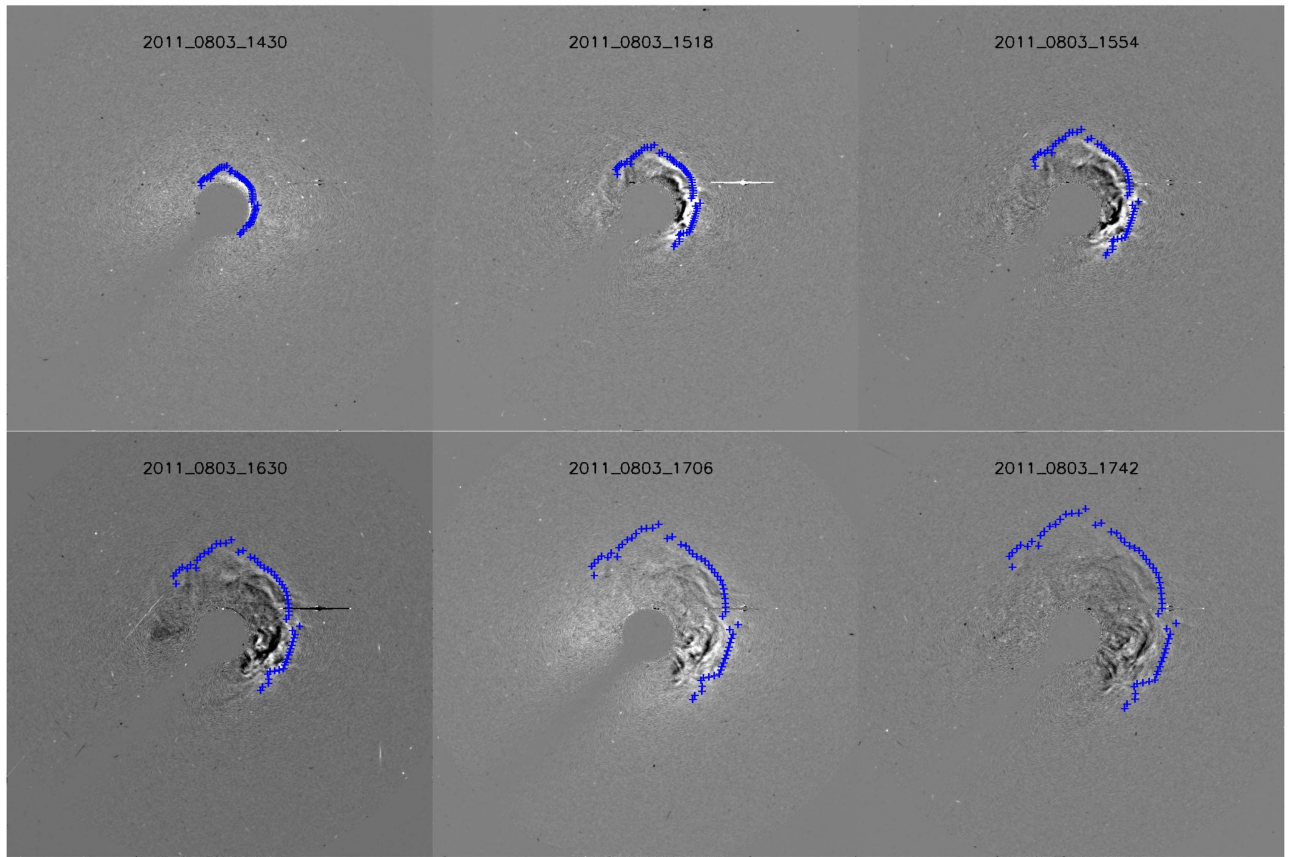
Figure 3. Tracking images of the 2011 August 3 CME in LASCO/C3 FOV (3.5–30 R_s).

eruption location based on *SOHO*/LASCO observations. However, we may roughly limit the eruption location in one of the four quadrants of the solar disk according to the recognized CPA and let the ice cream cone model refine the location through the fitting procedure. It should be noted that since the eruption location is not identified, iCAF cannot distinguish the frontside and backside CMEs, and an additional constraint from, e.g., extreme ultraviolet (EUV) observations of the solar disk, should be incorporated into the system in the future. Figure 4 shows the fitting result of the 2011 August 3 halo CME; the triangles are distributed based on the projected speeds at PAs (the PAs here are converted to start and span counterclockwise from the west of the Sun), and the dashed curve is obtained from the model fit based on the least-squares method. It is found that the curve matches well with most of the triangles. The derived 3D parameters are 979 km s^{-1}, 108°, and [13N, 9W], corresponding to the radial speed, the AW, and the eruption direction, respectively.

2.3. Module 3: Trajectory Reconstruction

CMEs will experience deflection during their propagation in coronae and interplanetary space. Here, we only consider the deflection of isolated CMEs. The previous two modules detect and track CMEs based on *SOHO*/LASCO/C2 and C3 coronagraphs covering the distance from 2 to 30 R_s, thus the CME direction in the corona has been obtained. Then, iCAF uses the deflection model (called DIPS; Wang et al. 2004, 2014) to reconstruct the trajectory of the CMEs in interplanetary space. In DIPS, the CME radial speed, the AW, and the initial longitude, combined with the solar wind speed,
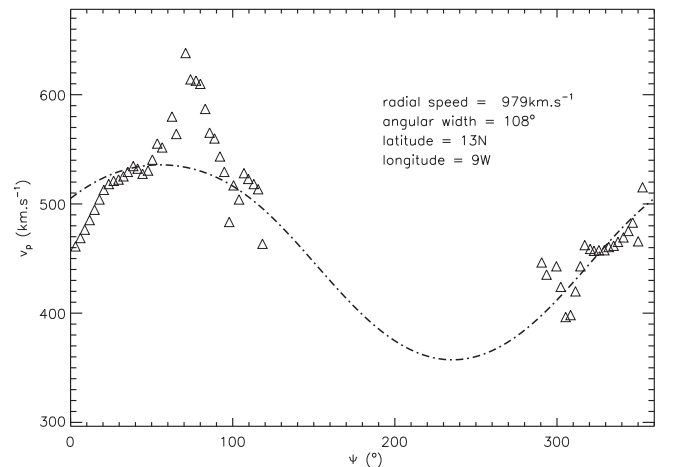
Figure 4. Ice cream cone model fit to the 2011 August 3 CME.

are required. In the current version, the solar wind speed, which can be distance-dependent, is set to be a default constant value of 400 km s^{-1}. Since the previous module uses a linear fit to derive the speed, which is a kind of average value within *SOHO*/LASCO FOV, we set the initial distance of the deflection of a CME to be 20 R_s, a roughly middle distance in the FOV of *SOHO*/LASCO. Although the deflection estimated by DIPS is only in the ecliptic plane, it is effective for meeting the needs of CME-arrival forecasting. Figure 5 shows the trajectory of the 2011 August 3 halo CME. The CME front is assumed to be an arc, which ends where two tangential lines crossing the solar center are separated by an
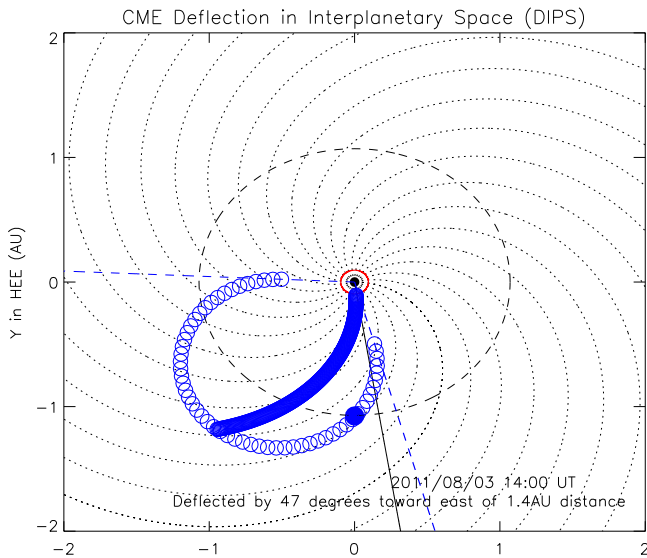
Figure 5. Trajectory of the 2011 August 3 CME in interplanetary space. The black solid line indicates the initial propagation direction, and the two blue dashed lines indicate the tangential lines.
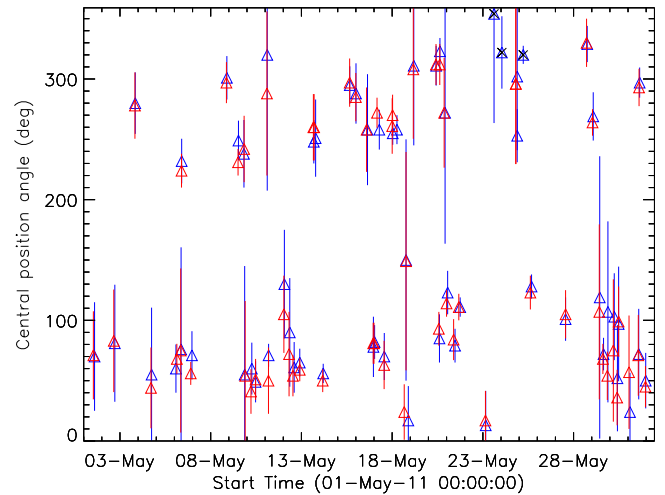

Figure 6. The CME overview map. The blue diamonds represent the data points of the CDAW catalog in time and CPA space and the red triangles represent the data points of iCAF. The vertical lines indicate the angular widths. The three CMEs missed by iCAF are denoted by the symbol X.

angle equal to the CME's AW. Here, the blue solid dot indicates the position of the Earth. According to the figure, this CME is found to encounter the Earth, consistent with the in situ observations.

3. The Performance of iCAF

We design three plans to test the performance of the modules of iCAF: (1) a comparison of the 2D projected parameters of the detected CMEs in iCAF with those in the CDAW catalog; (2) a comparison of the ice cream cone model parameters with those by the GCS model; (3) a check of the in situ data near the Earth to confirm whether or not the detected CME hit the Earth, and then an estimate of the success rate of the iCAF arrival prediction. The last test is the final aim of our work, through which the significance of the influence of the deflection in interplanetary space on the CME-arrival forecasting is assessed.

3.1. Test the CME Detection

We select the CME events from 2011 May. Here, we do not consider the CMEs in the catalog that are noted as weak or very weak: these kinds of CMEs are supposed to have little effect on space weather. We first design a CME overview distribution map (Figure 6), in which the data points are distributed by their first-appearance time and CPA space. The red triangles and blue diamonds represent the parameters provided by iCAF and the CDAW catalog, respectively, and the vertical lines indicate the corresponding AWs. It is found that the distributions for both are similar, and 95% (59/62) of the major CMEs in the catalog are detected by iCAF. However, the red lines are always shorter than the blue lines, indicating that the iCAF AWs are smaller than those in the catalog. This is reasonable because the faint edges of CMEs can be inspected by humans, but are not as easy to inspect for an automatic technique. The three CMEs missed by iCAF are denoted by the symbol X in the figure; two of them have speeds less than the speed limitation, i.e., $100 \, \mathrm{km \, s^{-1}}$, in our automatic detection, and the other one has an AW equal to the angular limitation, i.e., 15°.

A more detailed comparison of the parameters provided by iCAF and the CDAW catalog is given in Figure 7. Panel (a) plots the differences of the first-appearance time, in which the solid line indicates that the first-appearance time of a CME obtained by iCAF is equal to the first-appearance time in the CDAW catalog and the red dashed line indicates the average value of the differences. It is found that 72% of the diamonds are above 0 and the average value of the differences is about 33 minutes, indicating there is an advanced first-appearance time of about a half-hour given by iCAF. Such differences can be seen more clearly in panel (e), in which the bin size of the histogram is set to be 24 minutes, 2 times the temporal resolution of *SOHO*/LASCO instrument. We find that 25% of the data points are in the range of ±24 minutes near the zero (this range is marked by two dotted lines), and 63% are in the range of ±60 minutes (marked by two dashed lines). The comparison of the CPA is plotted in panel (b), in which the black line is the diagonal fit and the red dashed line is a linear fit. It is found that the correlation coefficient between the two sets of CPAs is 0.96, and the slope of the linear fitting line is about 0.99, indicating that they are quite consistent with each other. In panel (f), the histogram of the differences of the two sets of CPAs, whose bin size is set to 9°, which is 3 times the PA resolution in the CME detection module, is concentrated in the zero, with 68%(87%) in the range of ±9° (±20°) and the average value of the differences equal to 3°. For the comparison of the AWs in panel (c), 64% of the diamonds are beneath the diagonal line, and the slope of the linear fitting line is about 0.8, indicating that the AWs recognized in the automatic detection are on average 20% smaller than those detected by human inspection. In the corresponding histogram in panel (g), 38% (78%) of the differences of the two sets of AWs are in the range of ±9° (±30°), and the average value of the differences is about 11°. For a comparison of the CME speed, we take the linear speed in the CDAW catalog, which is measured for the fastest moving segment of the CME leading edge, and the maximum speed among all the PAs of a CME in iCAF. The slope of the linear fitting line in panel (d) is 0.87, indicating the 13% smaller estimation of the CME speed in iCAF. Panel (h) plots the histogram of the relative differences of the two sets of speeds, in which a relative difference is
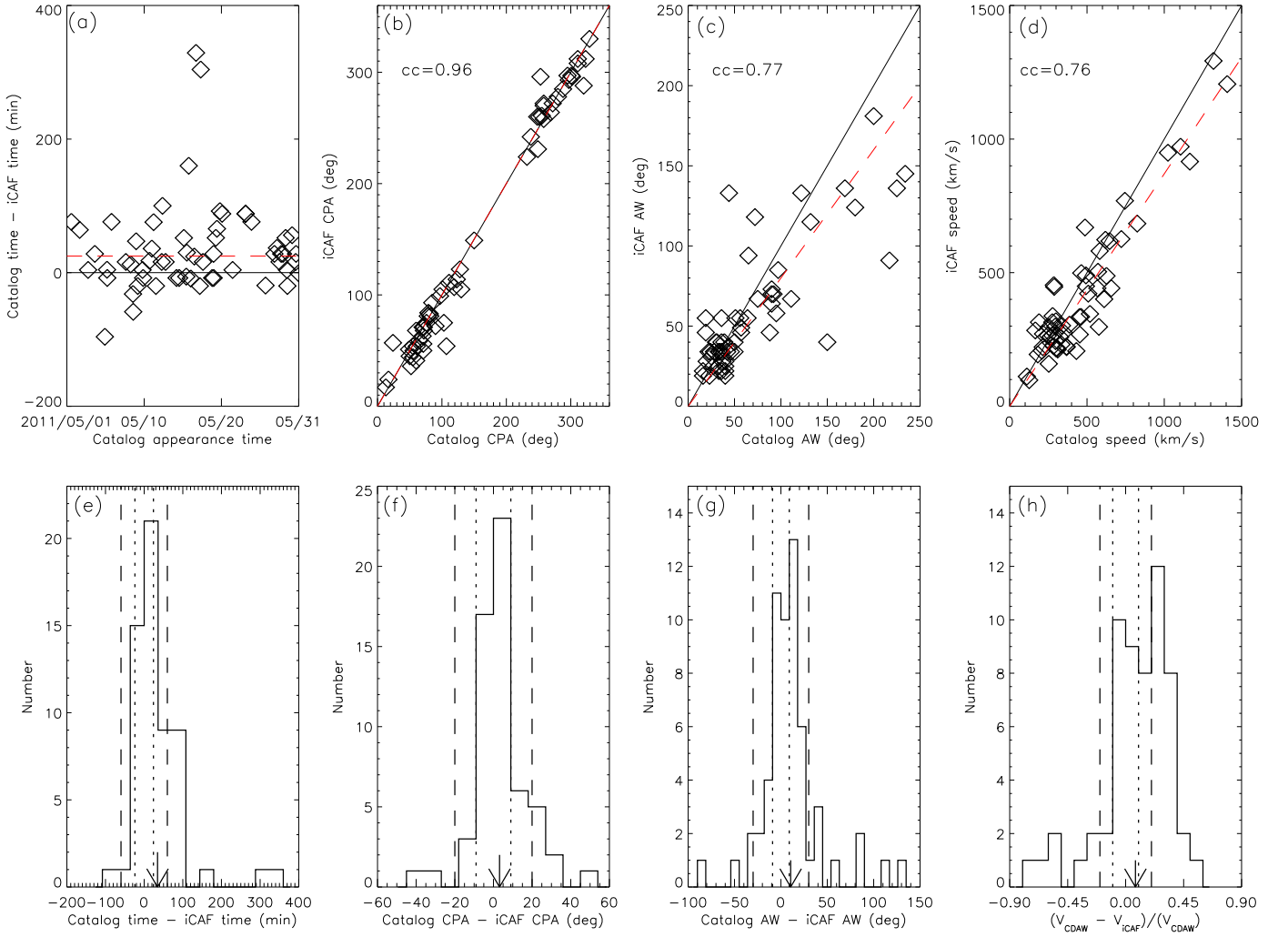
Figure 7. Comparison of the 2D projected parameters provided by both iCAF and the CDAW catalog. The solid black lines in the upper panels indicate the theoretical relationship that the two sets of parameters are equal to each other. The red dashed line in panel (a) indicates the average value of the data points, but in panels (b)–(d), which start from the zero, indicate a linear fit. In each lower panel, the bin size of the histogram is set to be 24 minutes, 9°, 9°, and 0.1. The arrow in panels (e)–(g) denotes the average value of differences of the two sets of first-appearance times, for CPAs and AWs. Panel (h) shows the histogram of the relative differences of the two sets of speeds, and the arrow indicates the position of the average value of the relative differences. Additionally, the dotted and dashed lines in the lower panels indicate the ranges discussed in Section 3.1.

derived by Equation (1) with V_{CDAW} as the speed of a CME in the catalog and V_{iCAF} as the speed in iCAF. It is found that the average value of the relative differences is about 0.06. Moreover, 32% (49%) of the data points are in the range of ±0.1 (±0.2).

$$\text{relative difference} = \frac{V_{CDAW} - V_{iCAF}}{V_{CDAW}}. \tag{1}$$

In this module, iCAF gives an earlier first-appearance time and a smaller CME speed than the CDAW catalog. Figure 8 describes this influence on a CME at $30\,R_s$ by moving the first-appearance time forward by 30 minutes and reducing the speed by 13%. It is found that the influence is not significant because the height differs from $26.6\,R_s$ to $33.3\,R_s$, with the original CME speed varying from 100 to 3100 km s^{-1}. In summary, the 2D projected parameters provided by iCAF are quite consistent with those from the CDAW catalog, though there are some slight differences in first-appearance time, AW, and speed.
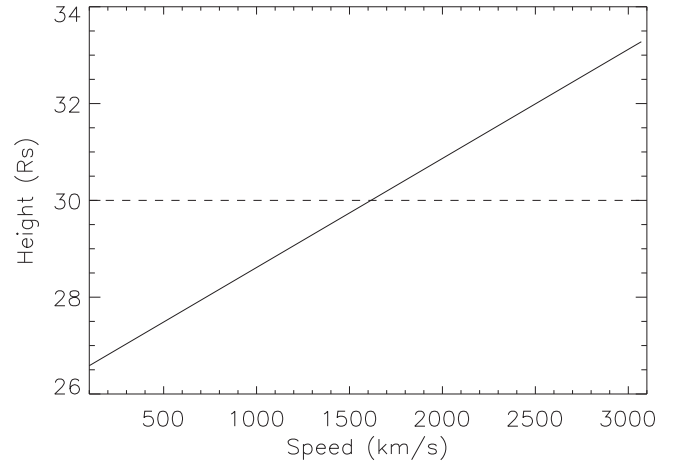
Figure 8. The plot of the height of a CME, which is initially supposed to reach the distance at $30\,R_s$, by moving the first-appearance time forward by 30 minutes and reducing the speed by 13%.

Table 1
38 Selected Frontside Halo CMEs

| No. | CME date & time | 3D Parameters | | | | | | Earth-arrival | |
| | | GCS Model | | | Ice Cream Cone Model | | | iCAF Prediction | Observation |
		direction	width	speed	direction	width	speed		
1	2010/02/07 03:54	E06, S7	81	481	E06, S11	80	379	Y	Y
2	2010/08/07 18:36	E36, S6	83	779	E44, N0	85	751	N	Y
3	2010/08/14 10:12	W42, S11	119	864	W34, S17	74	615	Y	N
4	2010/12/24 15:36	W35, N39	112	856	W80, N27	121	748	N	N
5	2011/02/14 18:24	W8, N1	61	365	W0, N40	66	313	Y	Y
6	2011/02/15 02:24	W5, S7	140	764	E9, S5	97	590	Y	Y
7	2011/03/07 20:00	W34, N33	104	1933	E9, S11	74	891	N	N
8	2011/06/02 08:12	E30, S3	92	961	E30, N16	131	1248	N	Y
9	2011/06/07 06:49	−1	−1	−1	E21, N0	131	1101	N	N
10	2011/06/21 03:16	E20, N7	93	964	W80, N0	156	1441	Y	Y
11	2011/08/03 14:00	W10, N12	124	925	W9, N13	108	979	Y	Y
12	2011/08/04 04:12	W36, N24	107	−1	W61, N34	160	1633	Y	Y
13	2011/08/09 08:12	W45, N16	133	1594	W40, N17	148	1401	Y	N
14	2011/09/06 02:24	−1	−1	−1	E21, N45	97	469	Y	Y
15	2011/09/06 23:05	W41, N19	116	901	W21, N5	120	944	Y	Y
16	2011/09/22 10:48	E72, N6	131	1823	E64, S11	108	1667	N	N
17	2011/09/24 12:48	E47, N6	119	1768	E43, N0	143	1109	N	Y
18	2011/09/24 19:36	−1	−1	−1	E67, N5	138	1617	N	N
19	2011/10/22 01:25	−1	−1	−1	E61, N5	160	2002	N	N
20	2011/10/22 10:24	−1	−1	−1	W17, N22	120	1105	Y	Y
21	2011/10/27 12:00	E42, N26	51	−1	E4, N32	32	540	N	N
22	2011/11/09 13:36	E36, N24	172	1074	E40, N45	154	1109	N	Y
23	2011/11/26 07:12	W35, N17	177	900	W17, N10	107	926	Y	Y
24	2012/01/02 15:12	−1	−1	−1	W42, S11	80	640	Y	Y
25	2012/01/16 03:12	E56, N40	124	956	E44, N5	80	564	N	N
26	2012/01/19 14:32	E17, N43	142	1091	E9, N21	131	1003	Y	Y
27	2012/01/23 04:00	W16, N41	193	1906	E4, N33	136	2003	N	N
28	2012/01/26 04:32	W71, N56	85	1033	W80, N5	135	660	N	N
29	2012/01/27 18:27	W78, N27	179	1807	W51, N39	131	1493	Y	Y
30	2012/02/09 21:17	E42, N29	79	648	E67, N5	114	647	N	N
31	2012/02/10 20:00	E25, N20	74	583	E32, N22	74	489	N	Y
32	2012/02/23 08:12	W61, N28	135	442	W74, S22	142	763	Y	Y
33	2012/03/05 04:00	−1	−1	−1	E4, S11	131	954	Y	Y
34	2012/03/07 00:24	E36, N33	140	2012	W22, S34	166	2072	Y	Y
35	2012/03/09 04:26	W1, N6	73	1188	E4, S40	83	1618	N	N
36	2012/03/10 18:12	W16, N18	107	1271	E4, N16	143	1871	Y	Y
37	2012/03/13 17:36	W37, N33	104	1525	W28, N16	131	1787	Y	Y
38	2012/04/09 12:36	W40, N12	95	892	W63, N22	124	595	Y	Y

Note. "−1" means there is no GCS model parameter, and "Y" and "N" correspond to the Earth-encountered and Earth-missed results, respectively.

### 3.2. Testing the 3D Parameter Derivation

Since CMEs are believed to be shaped like flux ropes, the performance of iCAF 3D parameter derivation can be tested by comparing the 3D parameters of the ice cream cone model to those of the GCS model. Shen et al. (2013, 2014) provided a list of the frontside halo CMEs along with some parameters from the GCS model (the propagation direction, the face-on width, and the speed).[8] We select the events for our comparison using two criteria: there must be no long-time data gap in SOHO/LASCO imaging data and no CME–CME interaction. Using these criteria, 38 events are eligible. We list them in Table 1, along with the corresponding ice cream cone model fits. Here, seven CMEs cannot be fitted by the GCS model due to the following reasons: the CME pattern was contaminated by

other transient structures, and the CME had a shape that differed from the shape of a flux rope. Additionally, since the estimation of the GCS model speed was performed for the CMEs recorded in at least three frames, the speeds of two fitted CMEs cannot be estimated because one has a data gap in STEREO images and the remaining one has a leading edge appearing in two frames in LASCO/C2 FOV.

We compare the 3D parameters of the CMEs that can be fitted by both models in Figure 9. For the latitude in panel (a), it is found that the two sets of latitudes are not quite consistent with each other, and the correlation coefficient is only 0.28. The slope of the dashed linear fitting line is about 0.64, indicating that most of the propagation directions fitted by the ice cream cone model are to the south of those fitted by the GCS model. Panel (e) plots the histogram of the differences. We find that 48% (68%) of the data points are in the range of ±9° (±20°), and the average value of the differences is 10°, on

---

[8] These events can be found at http://space.ustc.edu.cn/dreams/fhcmes
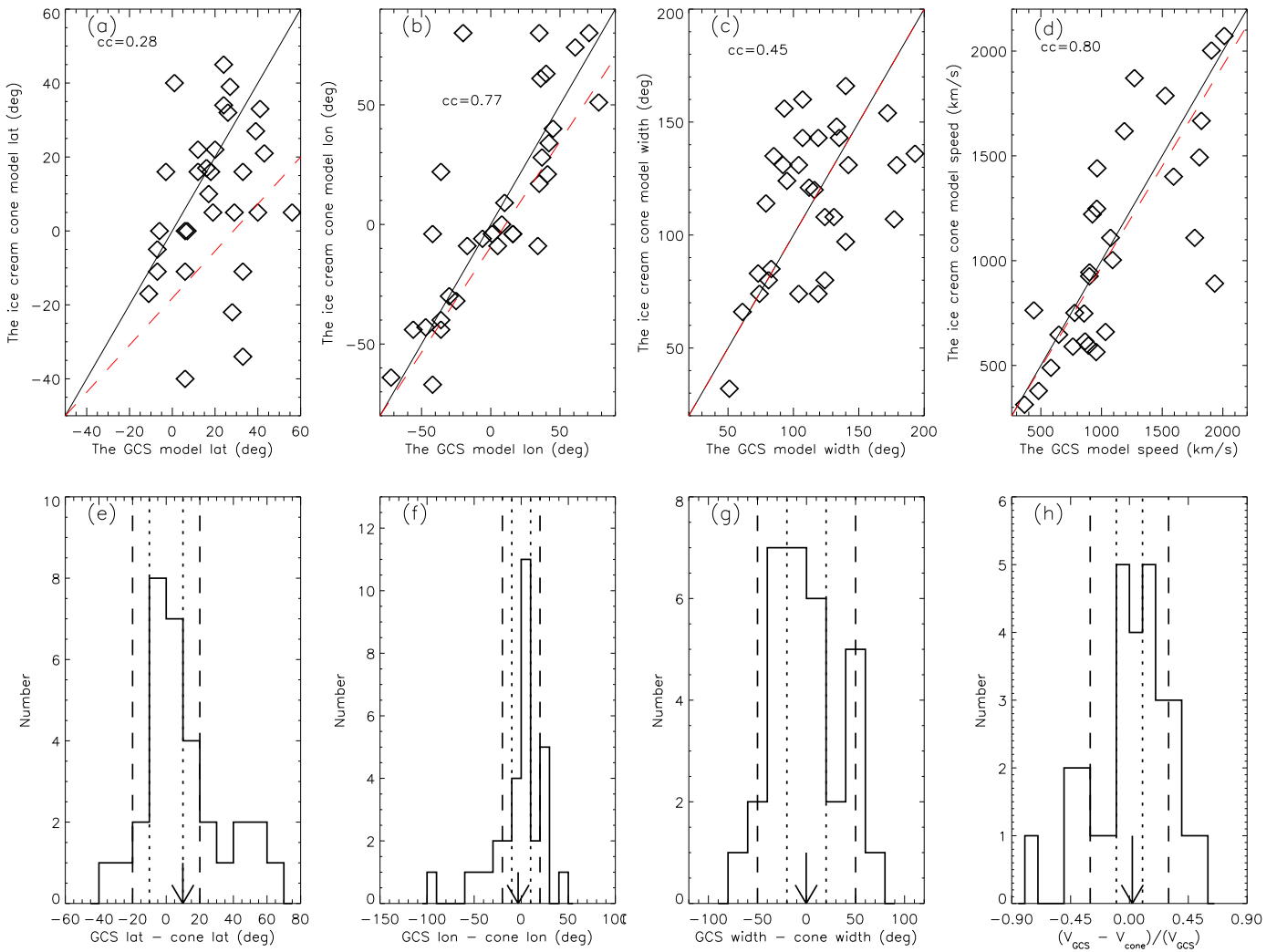
Figure 9. Comparison of the 3D parameters fitted by both the ice cream cone model and the GCS model. The positive value indicates a northern location for the latitude in panel (a) and a western location for the longitude in panel (b). In each upper panel, the black diagonal indicates that the two sets of parameters are equal to each other, and the red dashed line that begins at the bottom left point indicates a linear fit to the data points. In each lower panel, the bin sizes of the histogram are set to be 9°, 9°, 20°, and 0.1. The arrow indicates the average value of the differences of the two sets of latitudes, longitudes, and AWs in panels (e)–(f), and the average value of the relative differences of the two sets of speeds in panel (h). Additionally, the dotted and dashed lines indicate the ranges discussed in Section 3.2.

the right of the zero. However, the two sets of longitudes are much more consistent, with a correlation coefficient of about 0.77 (panel (b)). The slope of the linear fitting line is about 0.88, and 48% (71%) of the data points are in the range of ±9° (±20°), with the average value of the differences equal to −3° in panel (f). Panel (c) shows the comparison between the cone width and the face-on width of the flux rope. There is a weak correlation between the two sets of widths, with a correlation coefficient of about 0.45, and the linear fitting line is almost the diagonal line. We find that 58% of the AWs of the ice cream cone model are larger than those of the GCS model, and the average value of the differences is about −1° (panel (g)), indicating that there is no obvious trend of the prior AWs being larger or smaller than the latter. Additionally, 42% (87%) of the data points are in the range of ±20° (±50°) in panel (g). For the comparison of the speed in panel (d), the correlation coefficient of the two sets of speeds is about 0.8, and the slope of the linear fitting line is equal to 0.92. Panel (h) plots the histogram of the relative differences of the two sets of speeds, in which a relative difference is derived from Equation (2), with V_{GCS} as the speed of a CME fitted by the GCS model and V_{cone} as the radial speed

fitted by the ice cream cone model. The average value of the relative differences is about 0.04, and 52% (70%) of the data points are in the range of ±0.2 (±0.3). It is found that the differences in the speed are not significant due to the following reasons: the slope of the fitting line in panel (d) is very close to unity, and the average value of the relative differences is very small. Although the correlation coefficients in Figure 9 are not quite high, the histogram distributions concentrated in the zero indicate that it is still appropriate to use the ice cream cone model to roughly fit the CME 3D parameters:

$$\text{relative difference} = \frac{V_{GCS} - V_{cone}}{V_{GCS}}. \quad (2)$$

There are several reasons for the deviations of the iCAF 3D parameters from the GCS model fitting parameters. First, there are errors in the 2D projected parameters extracted by iCAF, which influence the ice cream cone model fit. Second, the rough limitation of the eruption location by the 2D CPA raises other errors. Figure 10 shows how well iCAF constrains the eruption location of a CME. In the figure, the dots represent the data points of the GCS model and the squares represent those
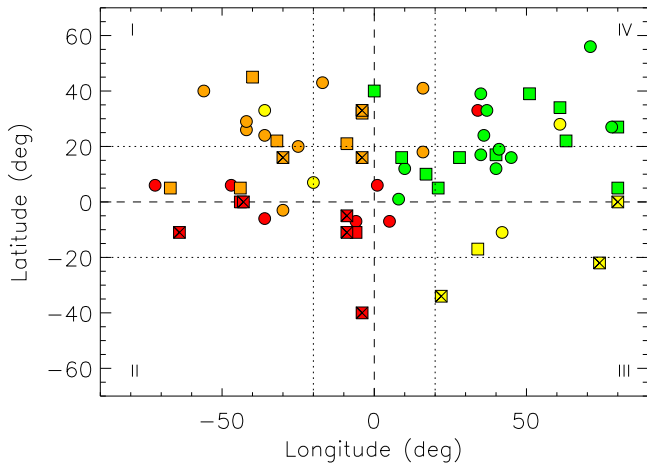
Figure 10. This figure shows how well iCAF constrains the eruption location of a CME based on its CPA. The dots and squares represent the data points of the GCS model and the ice cream cone model in latitude–longitude space, respectively, in which the positive value indicates a northern location for the latitude and a western location for the longitude. The orange color indicates that the corresponding 2D CPA of the CME is located in the first quadrant, which begins counterclockwise from the north of the Sun on the solar disk, followed by the red, yellow, and green. The horizontal and vertical dashed lines mark the ranges of latitude and longitude of about ±20°, respectively.

of the ice cream cone model in latitude–longitude space. The four different colors indicate that the corresponding CPA of the CME provided by the automatic detection is located in four different quadrants. From the distribution of dots we find that the GCS model can give inconsistent results. There are a total of 11 dots, including 3 orange dots, 5 red dots, and 3 yellow dots, located in a quadrant different from their corresponding squares, which have been marked with the symbol X. Considering a reasonable uncertainty of 20 degrees in both latitude and longitude as shown in panel (e) and (f) in Figure 9, we find that 9 of the 11 inconsistent data points are within the uncertainty.

3.3. Test the CME Arrival Prediction

Table 1 also lists the CME-arrival predictions by iCAF as well as confirmations by in situ observations. Among the 38 halo CMEs, 24 of them arrived at Earth (referred to as Earth-encountered CMEs) while 14 did not (referred to as Earth-missed CMEs). It is found that 19 of the Earth-encountered CMEs and 12 of the Earth-missed CMEs were successfully predicted by iCAF. The success rate is about 82% (31/38) and the error rate is about 18% (see Table 2). Furthermore, to test the importance of the deflection module in iCAF, we assume that the direction of a CME will not change during the propagation, i.e., there will be no deflection in interplanetary space, and compare the prediction results with those considering deflection. The results are listed in the parentheses in Table 2. It is found that 19 of the Earth-encountered CMEs and 5 of the Earth-missed CMEs are successfully predicted. The success rate reduces to 63%. Following the description of the deflection model in Wang et al. (2004), the curve in Figure 11, which is similar to Figure 7 in their paper, plots the deflection angle of CMEs with various radial speeds in the ecliptic plane at 1 au when the solar wind speed is set a constant value of $400\,\mathrm{km\,s^{-1}}$. A CME will be deflected eastward if it has a speed greater than the solar wind speed and will be reflected westward if its speed is lesser than the solar wind speed. In
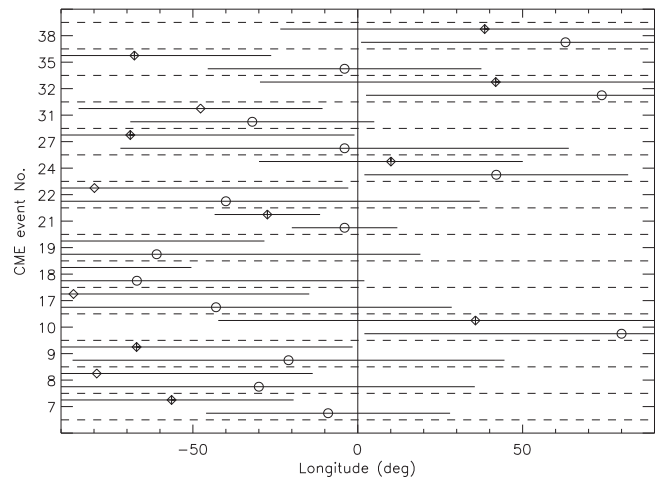
Table 2
Statistics of the CME Arrival Predictions and the Corresponding In Situ Observed Results

iCAF prediction (without deflection) Observation	Y	N
Y	19 (19)	5 (5)
N	2 (9)	12 (5)

Note. "Y" and "N" correspond to the Earth-encountered and Earth-missed results, respectively.
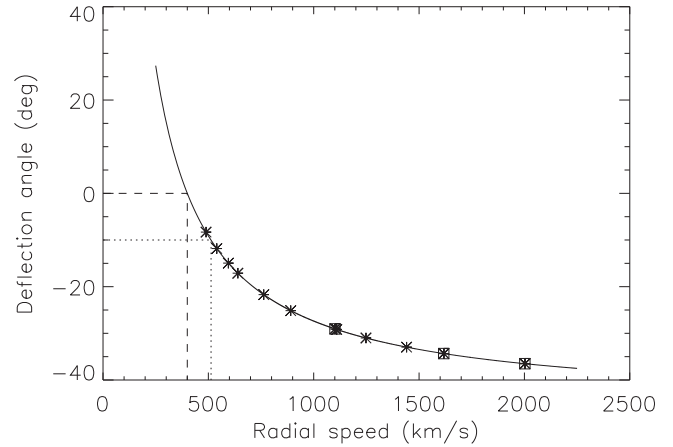
Figure 11. The deflection angle in the ecliptic plane at 1 au vs. the radial speed of CMEs. A positive value indicates a westward deflection, while a negative value indicates an eastward deflection. The symbols plot the deflection angles of the CMEs. The four symbols that are enclosed by the squares overlap because the CME ice cream cone model speeds of No. 9, 17 and 22 km s⁻¹; No. 19, 27 km s⁻¹; and No. 18, 35 km s⁻¹, are very close to each other in Table 1.

Figure 12. Variations of the longitudes of the CME propagation directions. We only consider the frontside deflection. The CME events are separated by the dashed lines and are detailed in Table 1. For each of the events, the circle indicates the initial longitude provided by the ice cream cone model of the CME and the diamond indicates the longitude after deflection. The horizontal lines indicate the ice cream AWs.

the figure, the symbols indicate the deflection angles of the CMEs whose arrival predictions without deflection are contrary to the predictions with deflection, and there are 15 such events among the 38 CME events. It is found that most of the deflection angles can reach 10° and even 40°, and the corresponding radial speeds are higher than $500\,\mathrm{km\,s^{-1}}$. Figure 12 illustrates how the deflection, which is indicated by

the variation of the longitude of the propagation direction, will influence the arrival predictions of these 15 CMEs. Here, the deflection angle is derived when one of the limb edges rather than the leading edge reaches a distance of 1 au. In the figure, the circle represents the initial longitude of a CME and the diamond represents the longitude after deflection. The horizontal lines crossing the symbols indicate the corresponding AWs. If a CME is predicted to encounter the Earth, the corresponding horizontal line should cross the middle vertical line where the Earth is located. All the arrival predictions in the figure are altered after deflection, and two data points move out of the axial range, i.e., to the backside of the Sun. Due to the eastward deflection (as seen in Figure 11), when a CME is initially located to the west of the Sun, the prediction is changed from Earth-missed to Earth-encountered, and vice versa for a CME to the east. Moreover, it is found that, among the 15 events, there are 11 events whose predictions with deflection are consistent with the in situ observations (denoted by the cross symbols in the diamonds in Figure 12, including two backside data points). The above analysis suggests that CME deflection in interplanetary space plays an important role for forecasting the arrival of CMEs at Earth.

4. Conclusions and Discussion

We develop an integrated CME-arrival forecasting (iCAF) system that is operated automatically and consists of modules of CME detection, 3D parameter derivation, and trajectory reconstruction based on coronagraph observations, to predict whether or not a CME will arrive at Earth. The performance of iCAF is tested for the following reasons: (1) 95% of the major CMEs in the CDAW catalog in 2011 May are detected by iCAF, and the 2D projected parameters provided by both methods are consistent with each other, with high correlation coefficients; (2) the correlation coefficients between the 3D parameters provided by the ice cream cone model and those from the GCS model are found to not be as high as those for the 2D parameters, but the zero-concentration of the parameter differences indicates that the iCAF-derived 3D parameters are acceptable, and the ice cream cone is an appropriate assumption to be used in CME-arrival forecasting; (3) the deflection angles of the tested CMEs are suggested to reach $10°$ or greater, and the success rate of the iCAF predictions is 82%, which is 19% higher than that of the predictions without deflection considered. In summary, the CME deflection in interplanetary space has significant influence on CME-arrival forecasting, and iCAF is a worthwhile project that considers deflection and makes real-time forecasting feasible. This system is currently undergoing tests at the Space Environment Prediction Center of the National Space Science Center, Chinese Academy of Sciences.

iCAF is preliminarily functional, but there are many possible future improvements. In the CME detection module, the recognition can be easily influenced by the noise: if a noisy feature is located near a CME feature, it will be recognized as a part of the CME, which will then differ the derived 2D parameters. In the 3D parameter derivation module, iCAF roughly limits the eruption location to one of the four quadrants of the solar disk according to the recognized CME CPA, and is unable to distinguish between frontside and backside CMEs. An additional constraint from the image data of the solar disk will be helpful. In the trajectory reconstruction module, the background solar wind is distance-independent, which could be changed to distance-dependent with the aid of other methods, e.g., the MHD numerical method (e.g., Shen et al. 2007, 2009, 2011). Lee et al. (2013, 2015a) showed that ambient structures from both solar wind streamers and small and slow CMEs may affect the propagation and arrival of a CME based on the WSA/ENLIL+Cone model. Thus, using more precise parameters for both CMEs and the background solar wind should improve the accuracy of iCAF forecasting. In the future, forecasting CME-arrival time will be integrated into iCAF, which can be used to further investigate how significantly CME deflection can influence CME-arrival time at Earth due to the curved front of the CME.

Appendix

In the CME detection module, iCAF implements the Hough transform technique to recognize bright-ridge features of CMEs in Jmap (time-height space). Figure 13 is an illustration of the Hough transform technique: a straight line in $[t, h]$ space can be parameterized by the slope v_0 and the intercept Δh_0; the Hough transform to this line is a point in $[v, \Delta h]$ space (the so-called Hough space), with the intensity being the integral of the intensity along the line in $[t, h]$ space; the local maximum in Hough space gives the parameters of the line. This module contains five procedures: the data processing, the Jmap derivation, the Hough transform, the CME identification, and the CME tracking. These are illustrated in detail based on the 2011 August 3 CME.

The data processing procedure is as follows. First, we input *SOHO*/LASCO/C2 "Quick Look" data, which are updated more quickly than needed for the real-time CME-arrival forecasting, and then we implement an exposure-time normalization, a noise filter (Llebaria et al. 1998), a running difference technique, and a polar transformation to process the data. Since the data can be recorded by different exposure times, they will be shown with different brightnesses and the normalization of the exposure time can remove this effect. By applying a noise filter, some bright point-like features such as cosmic rays, planets, and stars can be removed. In coronagraph images, a moving feature of a CME can be enhanced by a running difference technique. After a polar transformation, an $[x, y]$ LASCO/C2 FOV image will become a $[\theta, h]$ FOV image, with θ as the angle starting and spanning from the north of the Sun and h as the height measured from the solar limb.

The Jmap derivation procedure is as follows. If a Jmap at a certain PA cuts through a CME, an inclined bright ridge will be seen. Here, we set the angular resolution as $3°$, indicating that it will process 120 Jmaps at different PAs for the whole $360°$ in the plane-of-the-sky, and create each Jmap whose temporal
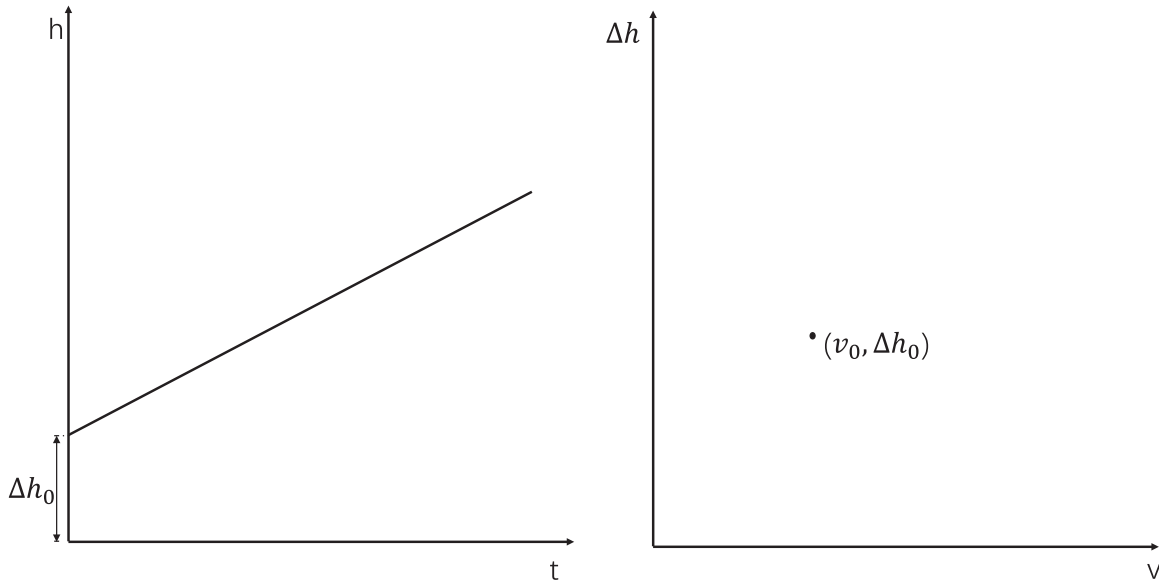
Figure 13. Illustration of the Hough transform. Left: the straight line is characterized by the slope v_0 and the intercept Δh_0. Right: $(v_0, \Delta h_0)$ is the corresponding point of the line in Hough space.

length is set to be 24 hr according to the observational time. A Jmap at a θ angle is derived by connecting the slices that are extracted from each of the $[\theta, h]$ images along the h direction at an angle θ from a starting time to an ending time 24 hr later. The bright ridge of the 2011 August 3 halo CME at 339° PA can be seen in the upper panel of Figure 14.

The Hough transform procedure is as follows. First, we select some data points, including the ridge whose pixel values are larger than the thresholds, i.e., the bright features, from a Jmap. The higher the height is from the solar limb, the less bright a CME feature becomes. Therefore, the thresholds are derived by Equation (3) at different heights with "avg" as the average value and "std" as the standard deviation of the pixel values at each of the heights. Currently, the "const" is set to be a constant value of 1.3, which can also be variable. Then, we apply the Hough transform to the selected data points and extract the linear information of the ridge feature according to the data points in the Hough space whose intensities are larger than another threshold. After that, the CME feature at a PA is recognized, and the 2D projected speed and the first-appearance time in LASCO/C2 FOV can be derived by fitting a straight line to a ridge that is formed by the highest data points from the recognized feature along the h direction, indicating the leading edge of a CME at this PA at different times. In the lower panel of Figure 14, the light blue symbols indicate the recognized Hough transform feature of the 2011 August 3 CME at 339° PA, with the red straight line indicating the linear fit. It is found that the red line slants slightly to the right and cannot match well with the leftmost edge of the feature, indicating that iCAF will give an earlier first-appearance time and a smaller speed for the 2011 August 3 CME at 339° PA:

$$\text{threshold} = \text{avg} + \text{const} \times \text{std} \qquad (3)$$

The CME identification procedure is as follows. The speed and the first-appearance time of a CME will differ slightly from
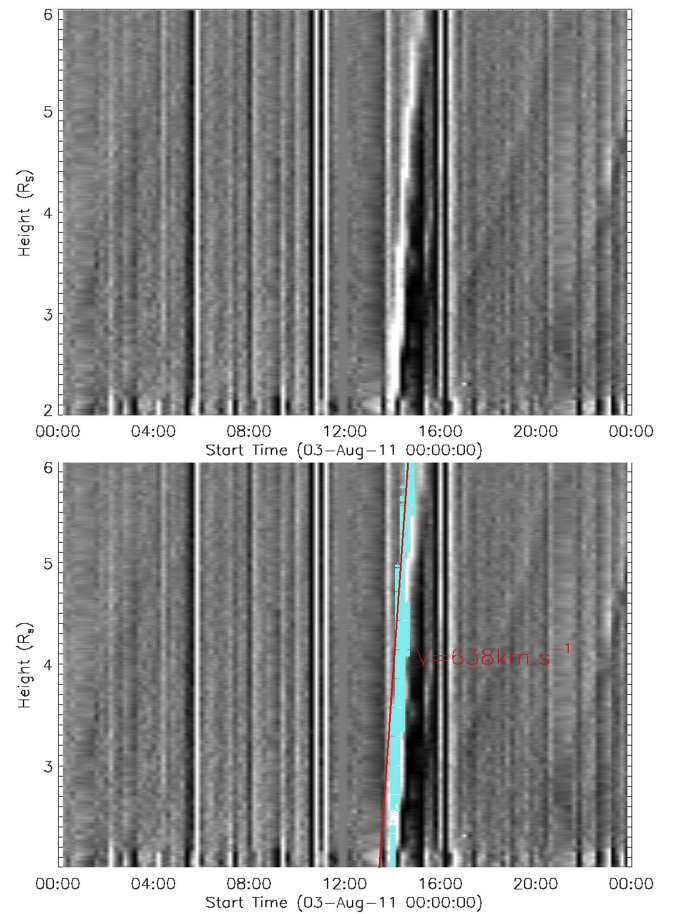
Figure 14. Jmap image and recognition result for the 2011 August 3 CME at 339° PA. Upper panel: since LASCO/C2 FOV is 2–6 R_s, the vertical axial range is equal to this range. A bright ridge can be seen. Lower panel: the blue symbols forming a ridge indicate the Hough transform recognition, and the linear fit to the recognized CME feature is shown by the red straight line.

11

angle to angle. Based on the CME identification procedure, iCAF identifies a CME from the scatters in time and PA space as drawn in Figure 2, in which the speeds are scaled by the colors. Starting from a data point, iCAF finds the nearest data point whose first-appearance time and speed are expected to be close to those of the initial data point. If the differences of the time, the PA, and the speed between both data points are within the limitations, i.e., 60 minutes, $10°$, and $200\,\mathrm{km\,s}^{-1}$, they will be combined as a cluster. Then, from that cluster, iCAF repeats the above procedure to find the next data point that is close to the cluster and has a similar speed. The iteration stops when no data point can be found to be combined with the cluster, i.e., the identification of a CME cluster is completed. The dashed rectangle in Figure 2 encloses the cluster after the iteration, which is the 2011 August 3 CME. After that, the 2D parameters (the CPA, the AW, the first-appearance time in LASCO/C2 FOV, and the speed) of a CME can be derived because the cluster has knowledge of the speed and time at the PAs spanned over the CME front. Here, we use the maximum speed, which is the speed of the fastest moving segment of the CME leading edge, to characterize a CME. The 2D parameters of the 2011 August 3 CME are $300°$, $190°$, 2011 August 3 13:12 UT, and $638\,\mathrm{km\,s}^{-1}$. Note that in the cluster of this CME, there may be multiple recognized results at a PA, as shown in Figure 2, because iCAF picks out all the data points in the Hough space whose intensities are larger than a threshold; then, the average values of the times and the speeds are used at this PA. iCAF will discard the CME whose angular width is smaller than $15°$, or whose speed is slower than $100\,\mathrm{km\,s}^{-1}$. In the figure, there is no other cluster covering more than the angular width of $15°$, so the remaining data points will be discarded.

The CME tracking procedure is as follows. Since iCAF has the first-appearance times and the projected speeds of a CME at the PAs spanned over the CME front, it can track a CME in coronagraphs. iCAF assumes that the speeds at all the PAs of a CME are constants and tracks the CME in the LASCO/C3 FOV. Figure 3 contains the tracking images at different times; the blue symbols mark the auto-detected leading edges of the CME, most of which match the observations well.

ORCID iDs

Bin Zhuang ⓘ https://orcid.org/0000-0002-5996-0693
Rui Liu ⓘ https://orcid.org/0000-0003-4618-4979

References

Arge, C. N., & Pizzo, V. J. 2000, JGR, 105, 10465
Berghmans, D., Foing, B. H., & Fleck, B. 2002, in ESA Special Publication, Vol. 508, From Solar Min to Max: Half a Solar Cycle with SOHO, ed. A. Wilson (Noordwijk: ESA), 437
Brueckner, G. E., Howard, R. A., Koomen, M. J., et al. 1995, SoPh, 162, 357
Byrne, J., Morgan, H., & Habbal, S. 2011, BAAS, 42, 23.01
Byrne, J., Morgan, H., & Habbal, S. R. 2012, in American Astronomical Society Meeting Abstracts, 220, 515.03
Cargill, P. J. 2004, SoPh, 221, 135
Chen, J., Howard, R. A., Brueckner, G. E., et al. 1997, ApJL, 490, L191
Chen, J., & Krall, J. 2003, JGRA, 108, 1410
Cid, C., Cremades, H., Aran, A., et al. 2012, JGRA, 117, A11102
Davis, C. J., Davies, J. A., Lockwood, M., et al. 2009, GeoRL, 36, L08102
Dere, K. P., Brueckner, G. E., Howard, R. A., Michels, D. J., & Delaboudiniere, J. P. 1999, ApJ, 516, 465
Fisher, R. R., & Munro, R. H. 1984, ApJ, 280, 428
Forbes, T. G. 2000, JGR, 105, 23153
Gopalswamy, N., Lara, A., Lepping, R. P., et al. 2000, GeoRL, 27, 145
Gosling, J. T., Bame, S. J., McComas, D. J., & Phillips, J. L. 1990, GeoRL, 17, 901

Hess, P., & Zhang, J. 2015, in AAS/AGU Triennial Earth-Sun Summit, Vol. 1, 212.06
Howard, R. A., Michels, D. J., Sheeley, N. R., Jr., & Koomen, M. J. 1982, ApJL, 263, L101
Howard, R. A., Moses, J. D., Vourlidas, A., et al. 2008, SSRv, 136, 67
Isavnin, A., Vourlidas, A., & Kilpua, E. K. J. 2014, SoPh, 289, 2141
Jahne, B. 1997, Practical Handbook on Image Processing for Scientific Applications (1st ed.; Boca Raton, FL: CRC Press)
Kaiser, M. L., Kucera, T. A., Davila, J. M., et al. 2008, SSRv, 136, 5
Kilpua, E. K. J., Pomoell, J., Vourlidas, A., et al. 2009, AnGeo, 27, 4491
Lee, C. O., Arge, C. N., Odstrcil, D., et al. 2015a, SoPh, 290, 1207
Lee, C. O., Arge, C. N., Odstrčil, D., et al. 2013, SoPh, 285, 349
Lee, H., Moon, Y.-J., Na, H., Jang, S., & Lee, J.-O. 2015b, JGRA, 120, 10237
Liewer, P. C., Dejong, E. M., Hall, J. R., & Lorre, J. J. 2005, AGU Fall Meeting, #SH14A-01
Llebaria, A., Lamy, P., & Malburet, P. 1998, A&AS, 127, 587
Lugaz, N. 2010, SoPh, 267, 411
Lugaz, N., Farrugia, C. J., Davies, J. A., et al. 2012, ApJ, 759, 68
Manoharan, P. K. 2006, SoPh, 235, 345
Mays, M. L., Taktakishvili, A., Pulkkinen, A., et al. 2015, SoPh, 290, 1775
Michalek, G. 2006, SoPh, 237, 101
Michałek, G., Gopalswamy, N., & Yashiro, S. 2003, ApJ, 584, 472
Möstl, C., Amla, K., Hall, J. R., et al. 2014, ApJ, 787, 119
Möstl, C., Rollett, T., Frahm, R. A., et al. 2015, NatCo, 6, 7135
Odstrcil, D., & Pizzo, V. J. 1999, JGR, 104, 28225
Olmedo, O., Zhang, J., Wechsler, H., Poland, A., & Borne, K. 2008, SoPh, 248, 485
Plunkett, S. P., Thompson, B. J., Howard, R. A., et al. 1998, GeoRL, 25, 2477
Qu, M., Shih, F. Y., Jing, J., & Wang, H. 2006, SoPh, 237, 419
Robbrecht, E., & Berghmans, D. 2004, A&A, 425, 1097
Rodriguez, L., Mierla, M., Zhukov, A. N., West, M., & Kilpua, E. 2011, SoPh, 270, 561
Rollett, T., Möstl, C., Isavnin, A., et al. 2016, ApJ, 824, 131
Sachdeva, N., Subramanian, P., Colaninno, R., & Vourlidas, A. 2015, ApJ, 809, 158
Schwenn, R., dal Lago, A., Huttunen, E., & Gonzalez, W. D. 2005, AnGeo, 23, 1033
Sheeley, N. R., Walters, J. H., Wang, Y.-M., & Howard, R. A. 1999, JGR, 104, 24739
Shen, C., Wang, Y., Pan, Z., et al. 2013, JGRA, 118, 6858
Shen, C., Wang, Y., Pan, Z., et al. 2014, JGRA, 119, 5107
Shen, C., Wang, Y., Wang, S., et al. 2012, NatPh, 8, 923
Shen, F., Feng, X., & Song, W. 2009, Science in China Series E: Technological Sciences, 52, 2895
Shen, F., Feng, X., Wu, S. T., & Xiang, C. 2007, JGRA, 112, A06109
Shen, F., Feng, X. S., Wang, Y., et al. 2011, JGRA, 116, A09103
Shi, T., Wang, Y., Wan, L., et al. 2015, ApJ, 806, 271
Srivastava, N., & Venkatakrishnan, P. 2004, JGRA, 109, A10103
Subramanian, P., Arunbabu, K. P., Vourlidas, A., & Mauriya, A. 2014, ApJ, 790, 125
Subramanian, P., Lara, A., & Borgazzi, A. 2012, GeoRL, 39, L19107
Thernisien, A. 2011, ApJS, 194, 33
Thernisien, A., Vourlidas, A., & Howard, R. A. 2009, SoPh, 256, 111
Thernisien, A. F. R., Howard, R. A., & Vourlidas, A. 2006, ApJ, 652, 763
Vourlidas, A., Lynch, B. J., Howard, R. A., & Li, Y. 2013, SoPh, 284, 179
Vršnak, B., Temmer, M., Zic, T., Dumbović, M., & Čalogović, J. 2016, in ASP Conf. Ser. 504, Coimbra Solar Physics Meeting: Ground-based Solar Observations in the Space Instrumentation Era, ed. I. Dorotovic, C. F. Fischer, & M. Temmer (San Francisco, CA: ASP), 209
Wang, Y., Chen, C., Gui, B., et al. 2011, JGRA, 116, 4104
Wang, Y., Shen, C., Wang, S., & Ye, P. 2004, SoPh, 222, 329
Wang, Y., Wang, B., Shen, C., Shen, F., & Lugaz, N. 2014, JGRA, 119, 5117
Wang, Y., Xue, X., Shen, C., et al. 2006, ApJ, 646, 625
Wang, Y., Zhang, Q., Liu, J., et al. 2016, JGRA, 121, 7423
Wang, Y. M., Ye, P. Z., Wang, S., Zhou, G. P., & Wang, J. X. 2002, JGRA, 107, 1340
Webb, D. F., Cliver, E. W., Crooker, N. U., Cry, O. C. S., & Thompson, B. J. 2000, JGR, 105, 7491
Xie, H., Ofman, L., & Lawrence, G. 2004, JGRA, 109, A03109
Xue, X. H., Wang, C. B., & Dou, X. K. 2005, JGRA, 110, A08103
Yashiro, S., Gopalswamy, N., Michalek, G., et al. 2004, JGRA, 109, A07105
Yermolaev, Y. I., & Yermolaev, M. Y. 2006, AdSpR, 37, 1175
Zhang, J., Dere, K. P., Howard, R. A., & Bothmer, V. 2003, ApJ, 582, 520
Zhao, X., & Dryer, M. 2014, SpWea, 12, 448
Zhao, X. P., Plunkett, S. P., & Liu, W. 2002, JGRA, 107, 1223